

# Elaboration of Superparamagnetic and Bioactive Multicore–Shell Nanoparticles ( $\gamma\text{-Fe}_2\text{O}_3\text{@SiO}_2\text{-CaO}$ ): A Promising Material for Bone Cancer Treatment

Xavier Kesse, Alexandre Adam, Sylvie Begin-Colin, Damien Mertz, Eric Larquet, Thierry Gacoin, Isabelle Maurin, Charlotte Vichery,\* and Jean-Marie Nedelec

Cite This: *ACS Appl. Mater. Interfaces* 2020, 12, 47820–47830

Read Online

ACCESS |

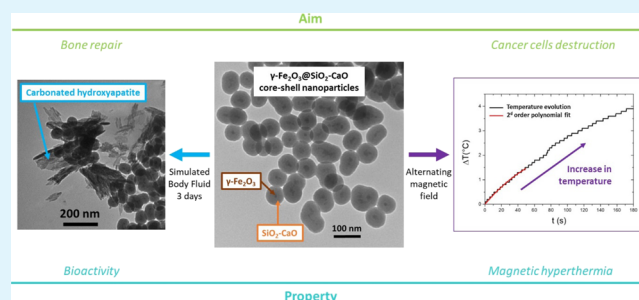
Metrics & More

Article Recommendations

Supporting Information

**ABSTRACT:** The past few decades have seen the development of new bone cancer therapies, triggered by the discovery of new biomaterials. When the tumoral area is small and accessible, the common clinical treatment implies the tumor mass removal followed by bone reconstruction or consolidation with a bioceramic or a metallic scaffold. Even though the treatment also involves chemotherapy or radiotherapy, resurgence of cancer cells remains possible. We have thus designed a new kind of heterostructured nanobiomaterial, composed of  $\text{SiO}_2\text{-CaO}$  bioactive glass as the shell and superparamagnetic  $\gamma\text{-Fe}_2\text{O}_3$  iron oxide as the core in order to combine the benefits of bone repair thanks to the glass bioactivity and cancer cell destruction through magnetic hyperthermia. These multifunctional core–shell nanoparticles (NPs) have been obtained using a two-stage procedure, involving the coprecipitation of 11 nm sized iron oxide NPs followed by their encapsulation inside a bioactive glass shell by sol–gel chemistry. The as-produced spherical multicore–shell NPs show a narrow size distribution of  $73 \pm 7$  nm. Magnetothermal loss measurements by calorimetry under an alternating magnetic field and in vitro bioactivity assessment performed in simulated body fluid showed that these heterostructures exhibit a good heating capacity and a fast mineralization process (hydroxyapatite forming ability). In addition, their in vitro cytocompatibility, evaluated in the presence of human mesenchymal stem cells during 3 and 7 days, has been demonstrated. These first findings suggest that  $\gamma\text{-Fe}_2\text{O}_3\text{@SiO}_2\text{-CaO}$  heterostructures are a promising biomaterial to fill bone defects resulting from bone tumor resection, as they have the ability to both repair bone tissue and act as thermoseeds for cancer therapy.

**KEYWORDS:** bioactive glass, superparamagnetic nanoparticles, sol–gel, coprecipitation, magnetic hyperthermia, bone regeneration, iron oxide



## INTRODUCTION

Nowadays, cancer is one of the major causes of death. It is estimated by the World Health Organization (WHO) that the number of people with this pathology will increase by 75% in the next two decades. If not detected sufficiently early, the primary tumor cells spread through the blood vessels and form new cancerous colonies (metastases) in different parts of the body. Among the organs affected, bones are the third-privileged site after the lungs and the liver.<sup>1</sup> As a consequence, a rapid resorption of the bone mass takes place because of an unbalanced bone remodeling process.<sup>2</sup> The patients can thus experience serious pain and pathological fractures which are highly detrimental for their quality of life.<sup>3</sup> Currently, chemotherapy, radiotherapy, and surgery with bone reconstruction or consolidation are the most common clinical treatments.<sup>4</sup> Despite great progress, these approaches are complicated, with numerous side effects<sup>5</sup> and the patient survival rate is quite low especially for young people dealing

with malignant bone tumors.<sup>6</sup> The development of alternative therapies that are more effective and less harmful is thus required.

Thanks to the development of nanotechnology, the past decades have seen significant breakthroughs in cancer therapies. Nanoparticle (NP)-mediated magnetic hyperthermia (MH) is one of the promising techniques for deep-seated tumor (such as bone tumor) treatment, as it exploits the tumor cell sensitivity to an increase in temperature over the physiological range. Under an alternating magnetic field (AMF), the magnetic NPs release heat in the tumor region

Received: July 15, 2020

Accepted: September 29, 2020

Published: September 29, 2020

which endamage the cancer cells.<sup>7</sup> Typically, a temperature between 41 and 46 °C alters the biological functions and physiological environment of the malignant cells leading to cellular death by apoptosis,<sup>8</sup> while a temperature above 46 °C induces their necrosis.<sup>9,10</sup> Iron oxide NPs (magnetite, Fe<sub>3</sub>O<sub>4</sub>, and maghemite,  $\gamma$ -Fe<sub>2</sub>O<sub>3</sub>) are the most promising candidates as thermoseeds for MH since the first experiments made on dog lymph nodes in 1957 by Gilchrist and co-workers.<sup>11</sup> They exhibit outstanding magnetic properties which allow them to have a high heating efficiency while being chemically stable in physiological media.<sup>12</sup> Furthermore, it is now well established that they are not toxic from a variety of studies based on their use in diagnosis and drug delivery.<sup>13</sup> Below about 30 nm in diameter, noninteracting iron oxide NPs are in a superparamagnetic state at ambient temperature, a magnetic behavior which is characteristic of monodomain ferro(i)-magnetic NPs above their blocking temperature ( $T_B$ ).<sup>9</sup> In this state, heat generation under an AMF is the consequence of two relaxation mechanisms: (i) Néel relaxation, where magnetization reversal along the easy axis induces a power loss and (ii) Brown relaxation in which the NPs physically rotate in order to align their magnetization along the magnetic field direction, with heat release through friction.<sup>9</sup> Another specificity of superparamagnetic iron oxide NPs (SPIONs) is that no magnetization is measured in the absence of a magnetic field (remanence and coercivity are zero), which is crucial for in vivo applications as residual magnetization induces NP aggregation, leading to a net reduction of their heating efficiency.<sup>14</sup> Note that the individual superparamagnetic NPs do have a permanent magnetic moment, but in the absence of a magnetic field, its fluctuation along the easy axis induces a zero net magnetization. For all these reasons (heating efficiency, nontoxicity, and biodegradability), SPIONs are nowadays preferential thermoseeds for MH as evidenced by the first adjuvant/therapeutic treatment commercialized in Europe by Magforce Nanotechnologies.<sup>15</sup>

As already pointed out, bone cancer treatments also include bone consolidation or repair. New therapy approaches should thus encompass both tumor destruction and bone regeneration. Bioactive glasses are attractive materials for bone regeneration as they chemically and strongly bind with the surrounding tissues when implanted in a bone defect and offer a biocompatible surface for bone tissue regrowth.<sup>16</sup> This biological linkage is achieved through the formation of a hydroxyapatite (HAp) layer onto their surface, the composition of which is close to the one of the mineral bone matrix.<sup>16</sup> Traditionally composed of SiO<sub>2</sub>, Na<sub>2</sub>O, CaO, and P<sub>2</sub>O<sub>5</sub> and elaborated by fusion (between 1000 and 1400 °C), bioactive glasses have been clinically used as an ossicle replacement in the eighties and more recently as bone fillers for small bone defects.<sup>17</sup> Lately, it has been reported that for a same composition, glasses in the ternary (SiO<sub>2</sub>-CaO-P<sub>2</sub>O<sub>5</sub>) and binary (SiO<sub>2</sub>-CaO) systems synthesized by the sol-gel process exhibit a higher bioactivity (HAp forming ability) than the one produced through the traditional high-temperature fusion route.<sup>18</sup> According to these authors, this result is related to their remarkable textural properties (high specific surface area arising from their porosity, about 150 m<sup>2</sup>/g, and high surface/volume ratio) which are intrinsic of the sol-gel polymerization process. Several experimental findings suggest that the specific surface area is the main parameter controlling the glass bioactivity. For example, Fan et al.<sup>19</sup> showed that the biomineralization process is enhanced for spherical 58S

bioactive glass NPs (BGNs) (60%mol SiO<sub>2</sub>, 36%mol CaO, and 4%mol P<sub>2</sub>O<sub>5</sub>) because of their large contact surface. Lei et al.<sup>20</sup> also reported that sol-gel-based BGNs exhibit a higher bioactivity with respect to micro-sized ones. Beside the advantages of the nanometric size, several in vivo studies in the literature highlighted the benefits of bioactive glass for bone repair in comparison to other bone graft substitutes such as HAp and/or apatite-wollastonite glass ceramic.<sup>21-23</sup> Indeed, a superior percentage of bone ingrowth along with a higher quality was observed, which might be attributed to the effect of the dissolution products (soluble silica and calcium ions) that stimulate the osteogenic cells to trigger the bone matrix mineralization. For all the above mentioned reasons, the elaboration of BGNs is of great interest for osseous reconstruction.

New therapeutic approaches, based on the use of the remarkable characteristics of iron oxide and BGNs, are thus interesting to investigate for bone cancer treatment as they would combine both the benefits of bone repair and cancer cell destruction through MH. Up to now, studies on bioactive and magnetic materials have been mostly focused on the synthesis of magnetic glass monoliths through several methods which do not allow for the fine control of their properties.

For example, Bretcanu et al.<sup>24</sup> reported the synthesis of ferrimagnetic glass ceramic materials in the system SiO<sub>2</sub>-Na<sub>2</sub>O-CaO-P<sub>2</sub>O<sub>5</sub>-FeO-Fe<sub>2</sub>O<sub>3</sub> by a melting procedure. They showed that the temperature used for melting controls the magnetic properties of the samples. However, their findings are not encouraging as the best sample elaborated exhibits a low heating capacity because of the crystallization of nonmagnetic hematite within the silicate matrix. In the work of Wang et al.,<sup>25</sup> the Fe<sub>2</sub>O<sub>3</sub>-CaO-SiO<sub>2</sub> glass ceramic elaborated by the sol-gel method and sintered at 950 °C for 1 h exhibits a rather low bioactivity if nucleating agents such as P<sub>2</sub>O<sub>5</sub> and TiO<sub>2</sub> are not added. Abbasi et al.<sup>26</sup> elaborated different bioactive ferrimagnetic glass ceramic materials by doping a solid state-derived 45S5 bioglass matrix with a variable proportion of sol-gel based strontium hexaferrite particles (SrFe<sub>12</sub>O<sub>19</sub>, from 5 to 20%wt). However, this study was not able to demonstrate efficiency for bone cancer therapy as the composite materials exhibit poor magnetic and bioactive properties.

In this work, magnetic and bioactive core-shell NPs with a core composed of superparamagnetic maghemite NPs and a bioactive glass (SiO<sub>2</sub>-CaO) shell have been synthesized by a combination of coprecipitation process and sol-gel chemistry. The main characteristics of these heterostructures in terms of physical features (size distribution, morphology, and specific surface area), along with their magnetic and bioactive properties have been evaluated and their heating capacity has been assessed under an external AMF. In addition, their cytocompatibility has been investigated in the presence of human mesenchymal stem cells (h-MSCs). To the best of our knowledge, this is the first time that such a multifunctional material, with few components, controlled physicochemical features and very interesting bioactive and magnetic properties have been obtained.

## ■ MATERIALS AND METHODS

**Materials.** Tetraethyl orthosilicate (TEOS, 99%), ammonium hydroxide solution (NH<sub>4</sub>OH 28.0–30%), calcium nitrate tetrahydrate (Ca(NO<sub>3</sub>)<sub>2</sub>·4H<sub>2</sub>O), iron (II) chloride tetrahydrate (FeCl<sub>2</sub>·4H<sub>2</sub>O, 99%), iron (III) chloride hexahydrate (FeCl<sub>3</sub>·6H<sub>2</sub>O, 99%), nitric acid solution (HNO<sub>3</sub>, 65%), and hydrochloric acid solution (HCl 32%)

were purchased from Sigma-Aldrich. Absolute ethanol (EtOH 99.5%) and acetone were obtained from VWR Chemicals. Citric acid monohydrate (99.5%) was purchased from Labogros.

**Synthesis of Maghemite ( $\gamma\text{-Fe}_2\text{O}_3$ ) NPs.** A colloidal suspension of maghemite NPs was prepared using the protocol already described by Vichery et al.<sup>27</sup> First, 11.4 mL of concentrated  $\text{NH}_4\text{OH}$  (14.8 M) was quickly poured into 36 mL of Fe(II) and Fe(III) chlorides acidic solution under vigorous stirring ( $\text{pH} = 0.06$ ,  $[\text{Fe(II)}] = [\text{Fe(III)}] = 0.54 \text{ M}$ ). The iron precursors coprecipitate instantly to form magnetite ( $\text{Fe}_3\text{O}_4$ ) particles which were recovered by magnetic decantation, washed twice with deionized water, and then dispersed in 4.9 mL of  $\text{HNO}_3$  (2 M); 12 mL of a  $\text{Fe}(\text{NO}_3)_3$  aqueous solution (1.5 M) were then poured onto the flocculate and the mixture was heated up to reflux for 30 min in order to fully oxidize magnetite into maghemite. Finally, the iron oxide particles were recovered and washed three times with acetone prior to their peptization in 30 mL of an aqueous nitric acidic solution ( $\text{pH} = 2$ ). A sonication (10 min) step and two centrifugation steps (6490 g/5 min) were performed in order to reduce the particle size dispersion.

**Maghemite NP Functionalization.** The smaller the particle size, the higher their surface reactivity.<sup>13</sup> Hence, the surface of the coprecipitated iron oxide particles was functionalized with citric acid to prevent their agglomeration. Citric acid is well known to enhance the colloidal stability of many oxide-based NPs by electrostatic repulsion in a large range of pH.<sup>28</sup> To do so, 15 mL of an aqueous citric acid solution (0.3 M) were added to 0.97 mL of the previously obtained ferrofluid (concentration of 73  $\text{mg}_{\text{Fe}_2\text{O}_3}/\text{mL}$ ) and the resulting solution ( $\text{pH} = 4.2$ ) was kept under stirring during 30 min. After three magnetic decantation/washing steps with acetone, the functionalized particles were dispersed by peptization in  $\text{H}_2\text{O}/\text{NH}_4\text{OH}$  (5 mL/0.5 mL). The resulting solution is called solution 1.

**Synthesis of Heterostructured NPs ( $\gamma\text{-Fe}_2\text{O}_3@/\text{SiO}_2\text{-CaO}$ ).** The growth of the bioactive glass shell around the maghemite NPs was performed following a modified Stöber route. First, two solutions were prepared separately at room temperature: solution 2 corresponds to 6.1 mL of TEOS (0.14 M) + 100 mL of EtOH, and solution 3 to 2 mL of concentrated  $\text{NH}_4\text{OH}$  (14.8 M) + 58.5 mL of  $\text{H}_2\text{O}$  + 87.5 mL of EtOH. After 10 min stirring, solution 1 (citrate maghemite colloid) was quickly poured into solution 3 under constant stirring. After 10 min, solution 2 was added to the previous mixture and the resulting solution was kept under stirring for 3 h. Then, 1.9 g of  $\text{Ca}(\text{NO}_3)_2 \cdot 4\text{H}_2\text{O}$  dissolved in 2 mL of deionized water were added and the final solution was stirred for 21 h. A brown precipitate was collected by centrifugation (6297 g/ 10 min) and washed several times with deionized water until a colorless supernatant was obtained. Finally, the recovered sample was dried in an oven at 60 °C and annealed in air at 650 °C for 3 h in order to promote the diffusion of  $\text{Ca}^{2+}$  ions inside the silica network.

**Physicochemical Characterization.** The morphology of bare maghemite and heterostructured NPs was characterized using a Hitachi H-7650 transmission electron microscope operating at 80 kV, on powder samples first dispersed in deionized water and deposited onto a transmission electron microscopy (TEM) grid. More than 200 particles were systematically analyzed using ImageJ software to determine particles size distributions.

High-resolution transmission electron microscopy (HRTEM) experiments were performed using a Titan Themis G3 field emission gun electron microscope operating at 300 kV with a C-Twin polar piece ( $C_s = 2.7 \text{ mm}$ ,  $C_c = 2.7 \text{ mm}$ , point resolution = 0.14 nm). Images were acquired on a  $4096 \times 4096$  pixels CETA II CMOS camera with an electron dose of  $d \approx 150 \text{ electrons} \cdot \text{Å}^{-2} \cdot \text{s}^{-1}$  at 660,000X magnification.

X-ray diffraction (XRD) patterns were recorded in the range  $2\theta = 20\text{--}80^\circ$  with a step of  $0.016^\circ$  using a PANalytical X'Pert Pro diffractometer for bare iron oxide particles and a D2 phaser (Bruker) diffractometer for the heterostructured samples, with the two instruments mounted in the Bragg–Brentano configuration and equipped with a Cu anode ( $\lambda_{\text{Cu}\alpha 1} = 1.5406 \text{ Å}$ ,  $\lambda_{\text{Cu}\alpha 2} = 1.5444 \text{ Å}$ ). The instrumental resolution function was obtained from a  $\text{LaB}_6$  NIST standard (SRM 660a).

The internal structure of the samples was also characterized by Fourier transform infrared spectrometry (FTIR, Nicolet 5700, Thermo Scientific) in transmission mode between 1400 and 400  $\text{cm}^{-1}$ . Measurements were performed on pellets made of KBr and particles in a weight ratio of 199:1.

The adsorption–desorption isotherms were recorded with a Micromeritics Tristar II PLUS sorptometer. The Brunauer–Emmett–Teller equation was applied to calculate the specific surface area.

The sample composition was determined by inductively coupled plasma-atomic emission spectroscopy (ICP-AES) using a ULTIMA-C spectrometer. A mixture of the sample powder (100 mg) and  $\text{LiBO}_2$  (300 mg) was melted for 5 min at 1100 °C in an induction furnace. The obtained melt droplets were then dissolved in  $\text{HNO}_3$  (50 mL, 1 M) and the volume of the solution was completed to 200 mL with 1 M  $\text{HNO}_3$ . Reference materials were prepared in the same way, while a pure  $\text{LiBO}_2$  solution (300 mg in 200 mL 1 M  $\text{HNO}_3$ ) was used as blank. The analytical wavelengths used for Si and Ca are  $\lambda = 251.611 \text{ nm}$  and  $\lambda = 317.933 \text{ nm}$ , respectively.

The zeta potential was measured using a Zetasizer nano apparatus (Nano-ZS, Malvern Instruments), after redispersion of the powder (citrate iron oxide) in deionized water and sonication for 10 min.

Magnetization measurements were performed on powder samples using a SQUID magnetometer (Cryogenic SX600). The samples were wrapped in food-grade transparent plastic film, which diamagnetic contribution was systematically subtracted. The fraction of magnetic material in each sample was derived from the iron content measured by ICP-AES. Magnetization versus magnetic field curves were recorded at 300 and 10 K and zero field cooled-field cooled (ZFC-FC) measurements were performed under 25G. The ZFC branch was obtained by cooling the sample down to the lowest temperature achievable by the magnetometer under a zero magnetic field. Then, a small external magnetic field (25 G) was applied and the magnetization of the sample was recorded upon heating up to room temperature. The FC branch has been obtained in the same way, except that the cooling step was performed under 25 G.

**In Vitro Bioactivity Study.** The apatite-forming ability was evaluated using the method reported by Kokubo et al.<sup>29</sup> Typically, 50 mg of sample powder were dispersed in a plastic beaker containing 50 mL of simulated body fluid (SBF), an alkaline solution mimicking the inorganic composition of human blood plasma, and kept in an orbital shaking incubator at 37 °C (N-BIOTEK). After 3 days of soaking, the particles were recovered by centrifugation, gently washed twice with deionized water, and finally dried at 60 °C before further characterization.

**Measurements of Specific Absorption Rate– MH Experiments.** Specific absorption rate (SAR) measurements were performed by a calorimetric method conducted on a MH apparatus (DM 100 instrument and DM applicator, Nanoscale Biomagnetics TM, associated with MaNIaC software). An adapted glass vial filled with 1 mL of an aqueous dispersion containing maghemite (powder) or heterostructured (powder/pellet) NPs with a Fe concentration of 1  $\text{mg}/\text{mL}$  was subjected to AMF ( $H = 300 \text{ G}$  and  $f = 536.5 \text{ kHz}$ ) and the thermal profile was monitored over 5 min.

**Cell Culture.** h-MSCs were extracted from metaphysic cancellous bones collected during hip arthroplasty surgical procedures on patients who had previously signed an authorization for the use of their bones for research purposes. The bones were collected in a solution of sterile phosphate-buffered saline (PBS) supplemented with 2% of heparin and transported immediately to the cell culture laboratory. After being washed with PBS, they were cut into small pieces and incubated for 15 min at 37 °C with 6 mL of minimum essential media (MEM) and 0.2 mL of collagenase. Then, bone pieces were filtered and washed with PBS in order to recover the h-MSCs, which were subsequently suspended in a standard marrow cell culture medium composed of MEM supplemented with gentamycin, sodium pyruvate, vitamins, nonessential amino acids, and fetal bovine serum. Cells were plated at  $20 \times 10^6$  cells in 25  $\text{cm}^2$  tissue culture flasks and incubated at 37 °C with 5% of humidified  $\text{CO}_2$ . After 3 days, the flasks were gently rinsed twice with PBS to remove the nonadherent cells.

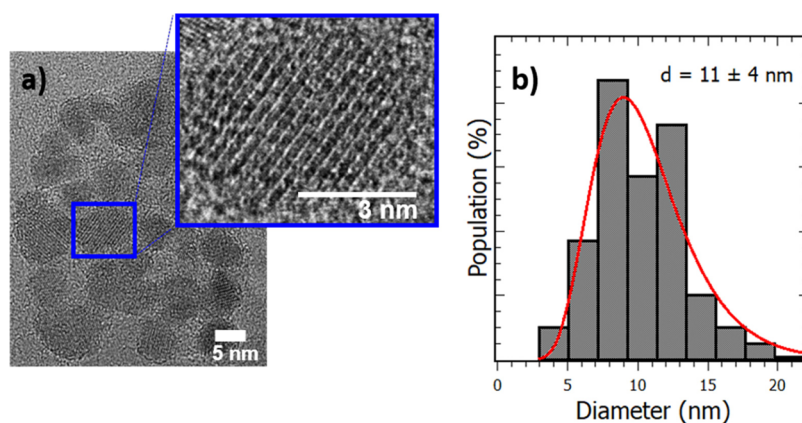


**Figure 1.** (a) Representative HRTEM image with a magnification in the inset and (b) size histogram of the magnetic NPs with the mean value and the variance of the distribution.

Adherent h-MSCs were fed by a weekly change of medium and expanded through one of three passages before being collected by trypsinization.

**In Vitro Cytotoxicity Tests.** The in vitro cytotoxicity tests were performed using the MEM cultured h-MSCs and sterilized samples (kept in an oven at 180 °C for 2 h). h-MSCs were seeded in a 24-well plate ( $5 \times 10^4$  cells/well), exposed to sample powders (concentration of 1 mg/mL) and then incubated for 1 week at 37 °C. h-MSCs cultured without powder were used as a control. After 7 days, the mitochondrial activity of the cells was evaluated using 3-(4,5-dimethylthiazol-2-yl)-2,5-diphenyl tetrazolium bromide (MTT) assays. For this test, 100  $\mu$ L of the MTT reagent at a concentration of 5 mg/mL in PBS was added to each well and the culture plates were incubated at 37 °C with 5% of CO<sub>2</sub>. After 3 h, the content of each well was carefully removed, leaving the powder and the cells at the bottom of the wells. Dimethyl sulfoxide (500  $\mu$ L) was then added in each well to lyse the cells and release the staining induced by the MTT reagent. After complete dissolution, the optical density (OD) of the wells was measured at 570 and 690 nm (spectrophotometer TECAN).

**Statistical Analysis.** Statistical analysis was performed using the Mann–Whitney nonparametric test with the Bonferroni correction,  $p < 0.05$  being considered as statistically significant. All of the experiments were performed in triplicate.

## RESULTS AND DISCUSSION

**Elaboration, Morphology, and Structural Characterization.** This study proposes the growth of a bioactive shell around preformed magnetic NPs to obtain bioactive and

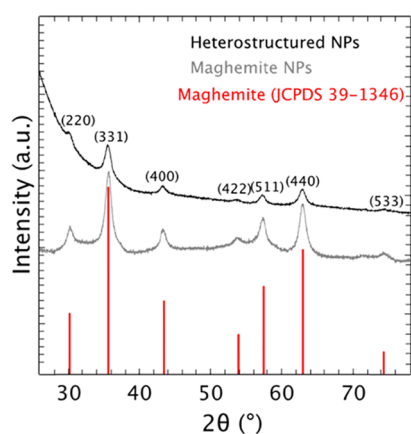


**Figure 2.** Overlay of the maghemite (gray, bottom) and the heterostructure (black, top) diffraction patterns.

magnetic heterostructures. One major advantage is the possibility to finely control and study separately the magnetic properties of the bare magnetic particles.

Maghemite NPs were elaborated using a two-step procedure involving precipitation from Fe(II) and Fe(III) salts under alkaline conditions and then the oxidation of the magnetic colloid under reflux in the presence of Fe(NO<sub>3</sub>)<sub>3</sub> used as a mild oxidizing agent. HRTEM images show that the particles exhibit a spheroidal morphology characteristic of the synthesis protocol (see Figure 1).<sup>13</sup> The average diameter evaluated by fitting the size histogram with a log-normal function is 11 nm (size dispersion of 36%). Thus, magnetic NPs with only a fair polydispersity in size have been obtained, presumably because of an overlap of the nucleation and growth processes during the addition of ammonia as magnetite formation follows the prediction of classical nucleation theory.<sup>30–32</sup> The observation of lattice fringes through the whole grain (see inset of Figure 1a) suggests that the particles are monocrystalline and present few defects.<sup>33</sup>

The diffraction pattern of the bare iron oxide particles shows Bragg peaks characteristic of a spinel structure, either maghemite ( $\gamma$ -Fe<sub>2</sub>O<sub>3</sub>) or magnetite (Fe<sub>3</sub>O<sub>4</sub>), see Figure 2. As the lattice parameter  $a$  differs for the two ferrites, its value has been accurately determined by fitting the experimental profile by full pattern matching (see Figure S1 in Supporting Information). The refinement yields  $a = 8.354 \pm 0.005$  Å, which is close to the theoretical lattice constant of natural maghemite ( $a = 8.352$  Å, JCPDS 39–1346) and quite far to the one of magnetite ( $a = 8.396$  Å, JCPDS 19–0629). Note that for a similar synthesis, Mössbauer spectroscopy experiments have confirmed the complete oxidation of the iron oxide particles.<sup>27</sup> Thus, it can be concluded that maghemite NPs have been obtained. Moreover, the coherence length evaluated from the (331) Bragg peak using the Scherrer formula is of about 9 nm, in good accordance with the HRTEM observations, confirming the monocrystalline character of the particles.

The formation of a bioactive shell around the maghemite NPs has been achieved through a modified Stöber method, which first required a functionalization of the particles with citric acid to ensure their dispersion in alkaline media prior to the sol–gel process. Once the silica shell is formed, the calcium salt is added into the reaction media. The bioactive SiO<sub>2</sub>-CaO shell is obtained after washing steps to remove counterions and unreacted species, and a thermal treatment at 650 °C to

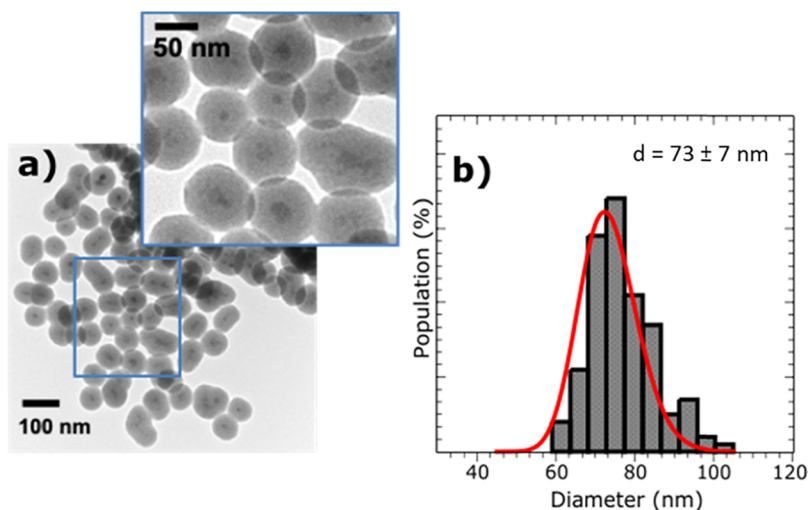


Figure 3. (a) Low-magnification TEM image and (b) size histogram of the  $\gamma\text{-Fe}_2\text{O}_3\text{@SiO}_2\text{-CaO}$  heterostructures.

Table 1. Nominal and Actual Composition of the Heterostructured Sample

	SiO <sub>2</sub>	CaO	Fe <sub>2</sub> O <sub>3</sub>
nominal composition (%molar)	76.2	22.4	1.4
actual composition (%molar)	86.2 ± 0.7	12.8 ± 0.1	1.02 ± 0.01

promote calcium diffusion and obtain a more uniform calcium distribution within the silica glass. This two-step process with a separate Ca incorporation allows avoiding side effects on the final particle textural properties (aggregation, nonsphericity, and high polydispersity in size) as reported in many studies.<sup>34–36</sup> Representative TEM micrographs of the heterostructured sample show that the composite particles exhibit a spherical shape with a multicore–shell structure (see Figure 3a). Such a result could be explained by the relatively good colloidal stability of the maghemite NPs in the reaction bath. Indeed, the functionalization of the magnetic NPs by citrate molecules induces an increase of the net surface charge because of the deprotonation of up to three carboxylic groups (pKa values of 3.13, 4.76, and 6.40 for citric acid). Thus, a rather good electrostatic repulsion between the citrated magnetic NPs can be obtained as evidenced by their zeta potential value of  $-29$  mV. Hence, one can see in Figure 3a that the bioactive glass shell has grown mostly around small

Table 2. Weight Percentage of Maghemite, Magnetization Saturation ( $M_s$ ) at 300 K, and Coercive Field ( $\mu_0H_c$ ) at 10 K for the Heterostructures and the Bare Maghemite Particles

sample	%wt Fe <sub>2</sub> O <sub>3</sub>	$M_s$ (300 K) (emu/g <sub>Fe2O3</sub> )	$\mu_0H_c$ (10 K) (G)
$\gamma\text{-Fe}_2\text{O}_3$	100	55 ± 2	210
$\gamma\text{-Fe}_2\text{O}_3\text{@SiO}_2\text{-CaO}$	3.65 ± 0.02	57 ± 1	210

aggregates and for a part around single particles. From the TEM images, we can also infer that no homogeneous nucleation of silica particles occurs and that all the magnetic particles are encapsulated. As illustrated in Figure 3b, the heterostructures exhibit a mean size of 73 and a size dispersion about 10%, proving that they are nanosized and quite monodispersed. In addition, they are nonagglomerated which means that the thermal treatment and the calcium salt addition in the reaction media 3 h after the beginning of the sol–gel process had no significant impact on their mean size and agglomeration state, as reported in our previous studies.<sup>37,38</sup> N<sub>2</sub> adsorption experiments (see Figure S2 in Supporting Information) showed that the heterostructures are not porous and display a specific surface area of 36 m<sup>2</sup>/g, which is very close to the theoretical value ( $S_{\text{theo}} = 37$  m<sup>2</sup>/g) calculated using

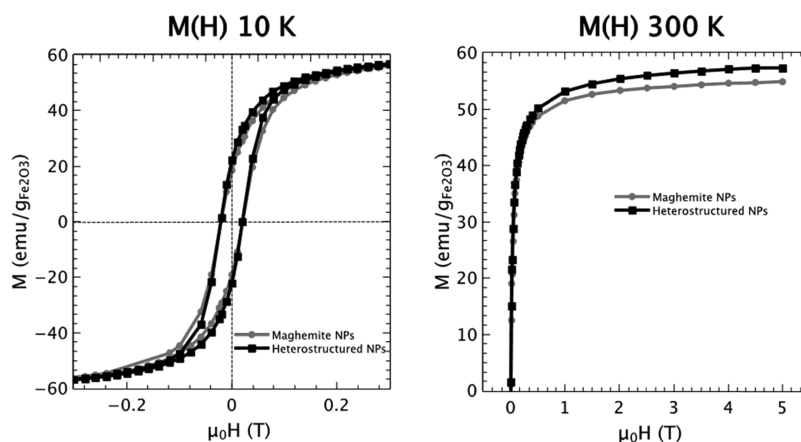


Figure 4.  $M(H)$  curves of maghemite (gray, circles) and heterostructured (black, square) NPs at 10 and 300 K.

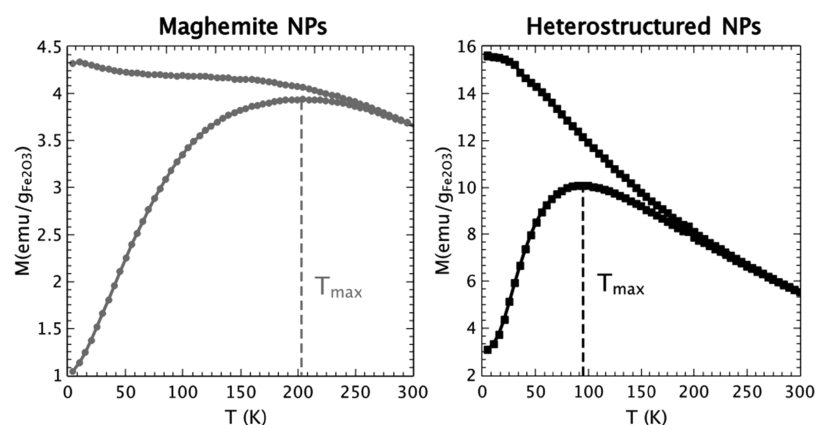


Figure 5. ZFC-FC magnetization curves of maghemite and heterostructured NPs recorded at 25 G.

Table 3. SAR Values, ILP Values, and Temperature Elevation after 1 min under AMF ( $\Delta T$ ) for Maghemite NPs (Colloidal Dispersion) and Heterostructured NPs (Colloidal Dispersion and Pellet Sample)

sample	SAR (W/g <sub>Fe</sub> )	ILP (nH.m <sup>2</sup> / kg)	$\Delta T$ (°C)
$\gamma$ -Fe <sub>2</sub> O <sub>3</sub> (colloidal dispersion)	757 ± 5	2.49 ± 0.01	7.5
$\gamma$ -Fe <sub>2</sub> O <sub>3</sub> @SiO <sub>2</sub> -CaO (colloidal dispersion)	159 ± 5	0.52 ± 0.01	1.5
$\gamma$ -Fe <sub>2</sub> O <sub>3</sub> @SiO <sub>2</sub> -CaO (pellet)	122 ± 5	0.40 ± 0.01	1.3

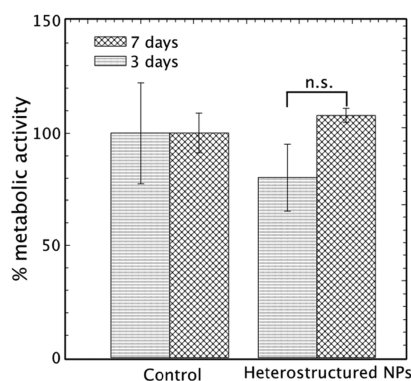


Figure 6. MTT results after incubation of the heterostructured NPs with h-MSCs during 3 and 7 days, (\*  $p > 0.05$ ). n.s.: not significant.

their size histogram. This hence confirms their nonagglomeration state.

As displayed in Figure 2, the XRD pattern of the heterostructured particles exhibits both a strong background corresponding to the diffuse scattering of the glass network and the characteristic peaks of maghemite. No other crystalline phase (like calcium and/or iron silicates) is evidenced confirming the chemical purity of the sample.

Similar to what was observed for the bare maghemite NPs, the Scherrer equation applied to the (331) diffraction peak leads to a coherence length value of about 10 nm, indicating the absence of significant particle coarsening on heating at 650 °C. It is important to point out that a sintering of bare maghemite particles occurs for annealing temperatures above 400 °C, leading to their phase transformation into hematite.<sup>27</sup> As no hematite peak can be detected in the heterostructures diffractogram, we can conclude that the iron oxide multiple cores within a SiO<sub>2</sub>-CaO particle should be separated from each other by a thin silica layer that prevents their coarsening and thus their phase transition into hematite.

Table 1 summarizes the heterostructures composition obtained by ICP-AES. About 57% of the initial Ca<sup>2+</sup> ions have been incorporated in the glass network, an insertion rate consistent with our previous findings.<sup>37</sup>

**Magnetic Properties.** Magnetization versus magnetic field curves were recorded at 10 and 300 K for both the maghemite and heterostructured NPs. The magnetization values were normalized with respect to the iron oxide mass in each sample. Figure 4 shows similar magnetic behavior for the single-phase and composite samples. Their  $M(H)$  curves at 10 K exhibit a small coercivity (see Table 2) while those recorded at 300 K present no hysteresis loop. The latter magnetic behavior is

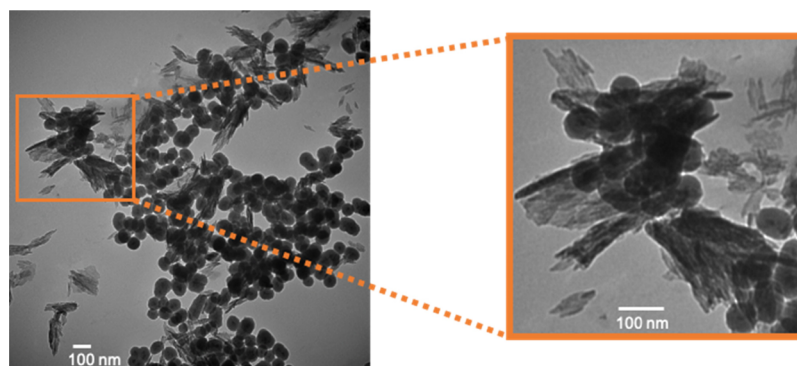
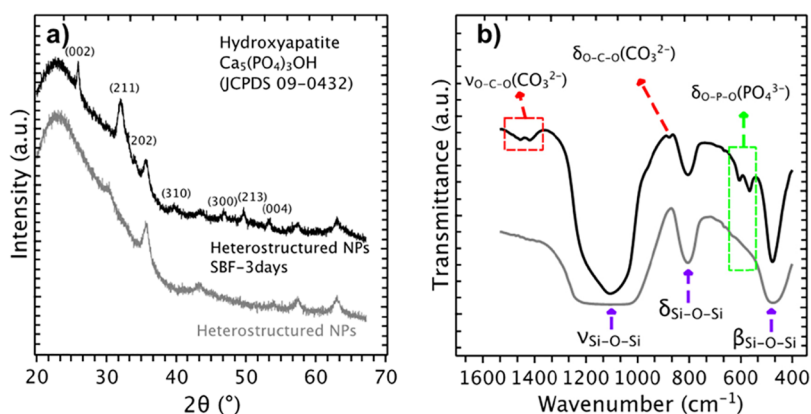


Figure 7. TEM image of the heterostructured NPs after 3 days of immersion in SBF.



**Figure 8.** (a) XRD profiles and (b) FTIR spectra of heterostructured NPs before (gray, bottom) and after (black, up) 3 days of immersion in SBF.

characteristic of particles in a superparamagnetic state.<sup>39</sup> The saturation magnetization ( $M_s$ ) values at 300 K (see Table 2) are much lower than the one of bulk maghemite ( $M_s = 75$  emu/g) because of an enhanced contribution of disordered surface spins (spin canting) as already described in other studies.<sup>33</sup> Also, one should note the  $M_s$  values for the bare magnetic particles and the heterostructures are not significantly different considering the uncertainties of weight measurements and determination of the  $\text{Fe}_2\text{O}_3/\text{SiO}_2\text{-CaO}$  mass ratio, meaning that the magnetic properties of the iron oxide particles have not been significantly altered by the growth of the shell and by the post-synthesis heat treatment. The  $M_s$  of the heterostructured NPs is of  $2.09 \pm 0.04$  emu per gram of sample (see Figure S3 in Supporting Information). It is interesting to compare this  $M_s$  value to those of other multifunctional materials described in the literature. A sol-gel derived bioactive glass mesoporous monolith with 3%mol of iron presents a  $M_s$  value of 0.15 emu/g,<sup>40</sup> another one with 5% mol of iron has a  $M_s$  value of 0.21 emu/g,<sup>41</sup> a mesoporous bioactive glass scaffold with 5%mol of iron exhibits a  $M_s$  value of 0.2 emu/g,<sup>42</sup> and another study presents one with a maximum value of 1.75 emu/g for a 9%mol of iron loading.<sup>43</sup> For all these composite materials, the iron precursor has been introduced during the sol-gel process and formation of the magnetic NPs occurred during a thermal treatment. There was thus no control of their nucleation and growth, leading to very small or poorly crystallized particles, and hence lower  $M_s$  values, despite a larger amount of iron compared to the heterostructures presented here (2.8%mol of Fe). Liu et al. synthesized a multifunctional magnetic mesoporous bioactive glass with 5%wt of magnetic NPs in a two-step process, first synthesizing the magnetic particles and then incorporating them in an acidic bioactive glass sol.<sup>44</sup> Despite the large  $M_s$  value of the bare magnetic NPs (59 emu/g), the composite sample only presents a  $M_s$  value of 1.44 emu/g. The authors tentatively assigned this finding to a partial dissolution of the magnetic NPs during the acidic hydrolysis step of the sol-gel process. In the present study, as the bioactive glass shell was grown in alkaline media, the integrity of the particles was preserved so that they retained their original magnetic properties. Note that the  $M_s$  value of the heterostructured NPs can be further increased to some extent by decreasing the thickness of the bioactive glass shell.

ZFC-FC measurements have also been performed to emphasize the transition from the blocked to superparamagnetic state when increasing the temperature. This transition is

characterized by  $T_B$ , over which the thermal energy overcomes the barrier energy between two magnetization states, allowing the fluctuation of the coupled magnetic moments along the easy magnetic axis. This situation results in a zero average magnetization. Actually, the maximum of the ZFC curves ( $T_{\max}$ ) corresponds to the  $T_B$  only in the case of an assembly of noninteracting and monodisperse particles.  $T_{\max}$  departs from  $T_B$  when the particles are polydispersed in size and when there are strong magnetic dipolar interactions between them.<sup>45,46</sup>

Figure 5 shows that the  $T_{\max}$  value is quite different for the bare maghemite NPs and the heterostructures, with  $T_{\max}$  values of 205 and 93 K, respectively. This discrepancy results mainly from different dipolar magnetic interactions which are also evidenced from the FC profiles. Indeed, the shape of the FC curves at low temperature is a good indication on the strength of these interactions as a plateau is characteristic of strongly interacting particles whereas a steep slope is specific of isolated particles.<sup>47</sup> FC curves thus confirm that the magnetic dipole interactions are far stronger for bare magnetic NPs than for the particles embedded in the  $\text{SiO}_2\text{-CaO}$  shell. Along with the noncoarsening of the magnetic particles after thermal annealing, this result gives another hint on the fact that the multiple iron oxide cores within a composite particle are separated by a thin silica layer.

**SAR Measurements.** The target application of these magnetic and bioactive heterostructures is to destroy cancer cells through MH. Calorimetric measurements under an applied AMF have thus been performed on aqueous dispersion of these magnetic heterostructures in order to assess the power dissipated by the particles, also called SAR or specific loss power. Measurements were carried out on bare maghemite particles and on heterostructures in order to investigate the impact of the  $\text{SiO}_2\text{-CaO}$  shell on heat release. The operating system not being under perfect adiabatic conditions (with thermal losses during measurement), the temperature profiles were recorded as a function of time and treated by means of the initial slope method (see Figure S4 in Supporting Information) in order to calculate the SAR. SAR is given per unit mass of iron ( $\text{W}\cdot\text{g}^{-1}$ ) and is expressed according to the relation:

$$\text{SAR} = \frac{C_p}{m(\text{Fe})} \left( \frac{\Delta T}{\Delta t} \right)_{t=0}$$

where  $C_p$  is the specific heat capacity of the magnetic suspension (here it corresponds to the one of water given

the sample dilution),  $m(\text{Fe})$  the mass of iron inside the sample, and  $\left(\frac{\Delta T}{\Delta t}\right)_{t=0}$  the initial temperature rising rate.

The interdependence of SAR with the magnetic field parameters (magnetic field frequency and amplitude) makes it difficult to compare the heating efficiency of the samples reported in the literature. Therefore, an alternative parameter, the intrinsic loss power (ILP, proportional to the SAR via the relation below) is conventionally used for this purpose.<sup>48</sup>

$$\text{ILP} = \frac{\text{SAR}}{H^2 f}$$

where  $H$  and  $f$  are the magnetic field amplitude and frequency, respectively. However, this parameter is reliable only for relatively low magnetic field amplitudes and frequencies.

Table 3 presents the SAR and ILP values of the maghemite and heterostructured NPs subjected to an AMF ( $H = 300$  G and  $f = 536.5$  kHz) for 3 min. The rise in temperature after 1 min of applied AMF is also reported to help visualize the heating capacity.<sup>49</sup> The bare maghemite NPs exhibit SAR and ILP values about 5 times higher than the ones of the heterostructures. This can be explained for a part by the presence of magnetic dipolar interactions in the heterostructures. Indeed, when SAR measurements are performed on aqueous dispersions at low concentration (1 mg<sub>Fe</sub>/mL), bare maghemite NPs are far away from each other and can be considered as noninteracting, whereas magnetic dipolar interactions should exist for the heterostructures as their core is composed of several Fe<sub>2</sub>O<sub>3</sub> NPs at a close distance. The impact of magnetic dipolar interactions on the heating power can be positive or detrimental, depending on the spatial arrangement of the magnetic particles. In the case of faceted particles, under an external magnetic field, dipolar interactions may induce a chain-like arrangement which promotes an increase of effective anisotropy, thus enhancing the heating power of the material.<sup>10,50,51</sup> These interactions have also been shown beneficial in nanoflower structures in which the crystallographic orientation of each primary particle is the same.<sup>52,53</sup> For these two examples, the collective behavior of the particles was found to improve their thermal efficiency. In the case of the multicore–shell NPs studied here, magnetic dipolar interactions are expected to have a detrimental effect, because the individual maghemite particles present disordered crystalline orientations, as pointed out by previous studies.<sup>54–56</sup> In addition, the low thermal conductivity of the SiO<sub>2</sub>–CaO shell induces a thermal shielding,<sup>57</sup> so that the heat generated by the magnetic NPs is not efficiently transferred to the surrounding media (silica heat capacity of 0.35 J/kg versus 4.18 J/kg for water). Nonetheless, interestingly, the ILP value of the heterostructures developed in this work lies in the range of already commercialized magnetic NPs (0.15–3.1 nH·m<sup>2</sup>·kg<sup>−1</sup>),<sup>48</sup> meaning they can be promising candidates for MH therapeutics.

Hyperthermia measurements were also performed on pellets made of pressed heterostructure powder in order to discriminate the contributions from Néel (heat produced by the magnetic relaxation of the particles' magnetization) and Brown (heat produced by the friction of the particles rotating in the media) relaxations. In the pellet configuration, particles are mechanically blocked so the only efficient mechanism is Néel relaxation.<sup>58,59</sup> Here, the SAR and ILP values summarized in Table 3 show a slight reduction for the pellet sample with respect to the colloidal dispersion. This result is consistent

with the literature as it is generally agreed that below 15 nm, Néel relaxation is the predominant contribution to SAR.<sup>60</sup>

**In Vitro Cytotoxicity.** The second target to assess the potential of these multifunctional particles as new therapeutic agents is their ability for bone reconstruction. For such biomedical applications, composite samples require further biological investigations, especially a proof of their cytocompatibility. We thus performed in vitro cytotoxicity tests as it is admitted that a material which is not toxic in vitro will also not be toxic in vivo.<sup>61</sup> To do so, MTT assays were used to assess the viability of h-MSCs after incubation with the heterostructured NPs during 3 and 7 days, respectively. According to Figure 6, the metabolic activity of h-MSCs does not change significantly in the presence of the particles, an observation confirmed by statistical analysis ( $p > 0.05$ ). Consequently, these heterostructured NPs can be considered as nontoxic.

**In Vitro Bioactivity.** The glass shell bioactivity was addressed by immersing the sample into SBF, a salt solution mimicking the inorganic part of human plasma and following the sample mineralization process (HAp formation).<sup>62</sup> Figure 7 shows a TEM image of the heterostructured NPs soaked in SBF for 3 days. A heterogeneous growth of crystals onto the particle surface can be observed. Their nature has been identified by XRD and FTIR spectroscopy. A closer inspection of the XRD pattern shown in Figure 8a shows new Bragg reflections characteristic of HAp (JCPDS 09–0432).<sup>38</sup> Furthermore, the presence of maghemite NPs peaks suggests their immobilization inside the heterostructures or within the apatite phase.

Although the FTIR spectrum of the raw heterostructured NPs only shows absorption bands of the silica network, the FTIR spectrum of the particles immersed in SBF clearly shows the appearance of two new bands, respectively, at 564 and 604 cm<sup>−1</sup> (Figure 8b) which can be assigned to HAp.<sup>63</sup> In addition, one can notice the presence of three additional bands located at 879, 1419, and 1458 cm<sup>−1</sup> which can be attributed to the O–C–O stretching and bending vibration of carbonate groups.<sup>64,65</sup> This indicates the formation of carbonated HAp, a mineral phase with a composition close to the one of natural bone. XRD and FTIR measurements thus prove that the heterostructured NPs elaborated in this study are bioactive. It should also be noted that in contrast to the works of Ebisawa et al.<sup>66</sup> and Ohura et al.,<sup>67</sup> the bioactivity of the nanocomposite is preserved despite the presence of iron oxide in the glass matrix.

## CONCLUSIONS

In this study, superparamagnetic and bioactive NPs with a multicore–shell structure were designed through a multistep approach. Maghemite NPs were prepared by a simple coprecipitation route and functionalized with citric acid to enhance their colloidal stability prior to being coated with sol–gel silica (modified Stöber protocol). Finally, the addition of calcium ions in the solution and their diffusion within the silica network upon postsynthesis annealing allowed the formation of a bioactive glass shell. Physical characterization showed that the heterostructures are not agglomerated and retain a nanometric size with a low polydispersity ( $73 \pm 7$  nm). An investigation of their heating capacity under an external AMF pointed out that they induce a temperature rise of water efficient enough to have a therapeutic effect on cancer cells. Furthermore, the in vitro bioactivity tests confirmed that the multifunctional material is bioactive after 3 days of immersion

in SBF, as evidenced by the precipitation of HAp on its surface. In vitro MTT assays in the presence of h-MSCs highlighted its cytocompatibility. Based on these findings, the elaborated  $\gamma$ -Fe<sub>2</sub>O<sub>3</sub>@SiO<sub>2</sub>-CaO heterostructures should be considered as promising for bone cancer treatment and should deserve further studies to improve their heating capacity by varying the size of the magnetic core and the synthesis parameter to obtain monocoreshell NPs with a thinner bioactive shell. Also, an experimental procedure which effectively demonstrates in vitro cancer cell destruction in the presence of such heterostructures in an AMF should now be conducted.

## ■ ASSOCIATED CONTENT

### SI Supporting Information

The Supporting Information is available free of charge at <https://pubs.acs.org/doi/10.1021/acsami.0c12769>.

Protocol for iron oxide lattice parameter determination; N<sub>2</sub> adsorption–desorption isotherm; M(H) curve of the heterostructured NPs plotted with the magnetization value in emu per gram of heterostructures and temperature evolution of bare maghemite NPs; heterostructured NPs and pure water under an AMF with  $H = 23.8$  kA/m and  $f = 536.5$  kHz along with fittings for SAR calculation (PDF)

## ■ AUTHOR INFORMATION

### Corresponding Author

Charlotte Vichery – CNRS, SIGMA Clermont, ICCF, Université Clermont Auvergne, Clermont-Ferrand F-63000, France; [orcid.org/0000-0003-2455-0704](https://orcid.org/0000-0003-2455-0704); Phone: +33 473405479; Email: [charlotte.vichery@sigma-clermont.fr](mailto:charlotte.vichery@sigma-clermont.fr)

### Authors

Xavier Kesse – CNRS, SIGMA Clermont, ICCF, Université Clermont Auvergne, Clermont-Ferrand F-63000, France

Alexandre Adam – Institut de Physique et Chimie des Matériaux de Strasbourg (IPCMS), UMR-7504 CNRS-Université de Strasbourg, Strasbourg 67034 Cedex 2, France

Sylvie Begin-Colin – Institut de Physique et Chimie des Matériaux de Strasbourg (IPCMS), UMR-7504 CNRS-Université de Strasbourg, Strasbourg 67034 Cedex 2, France; [orcid.org/0000-0002-2293-2226](https://orcid.org/0000-0002-2293-2226)

Damien Mertz – Institut de Physique et Chimie des Matériaux de Strasbourg (IPCMS), UMR-7504 CNRS-Université de Strasbourg, Strasbourg 67034 Cedex 2, France; [orcid.org/0000-0002-6745-8978](https://orcid.org/0000-0002-6745-8978)

Eric Larquet – Laboratoire de Physique de la Matière Condensée, Ecole Polytechnique, CNRS, IP Paris, Palaiseau 91128, France

Thierry Gacoin – Laboratoire de Physique de la Matière Condensée, Ecole Polytechnique, CNRS, IP Paris, Palaiseau 91128, France; [orcid.org/0000-0001-6774-3181](https://orcid.org/0000-0001-6774-3181)

Isabelle Maurin – Laboratoire de Physique de la Matière Condensée, Ecole Polytechnique, CNRS, IP Paris, Palaiseau 91128, France

Jean-Marie Nedelec – CNRS, SIGMA Clermont, ICCF, Université Clermont Auvergne, Clermont-Ferrand F-63000, France; [orcid.org/0000-0002-8243-6849](https://orcid.org/0000-0002-8243-6849)

Complete contact information is available at: <https://pubs.acs.org/doi/10.1021/acsami.0c12769>

## Author Contributions

X.K. carried out all the experiments except the cytotoxicity tests (Aurélié Jacobs), the magnetic measurements (I.M.), the HRTEM imaging (E.L.), and the SAR measurements (A.A. and D.M.) and processed all experimental data. C.V. designed the study and was in charge of overall direction and planning. All authors provided critical feedback and helped shape the research, analysis, and manuscript.

## Notes

The authors declare no competing financial interest.

## ■ ACKNOWLEDGMENTS

The operation AAP “ Nouveau Chercheur ” Nanoparticules bioactives et magnétiques pour le traitement de cancer et la régénération de tissus osseux is cofunded by the European Union as a part of the Fonds Européen de Développement Régional (FEDER) and by the Conseil Régional Auvergne-Rhône-Alpes. The authors wish to thank Christelle Blavignac from CICS for technical assistance (TEM) and Aurélié Jacobs (ICCF) for the cytotoxicity tests. D.M. acknowledges the Materials Institute Carnot Alsace (project ProtRemote) and the Canceropôle Est (project VIVIRMAG) for financial support. Electron microscopy work was supported by the French research programme “Initiatives de Recherche Stratégiques – projet Nan’eau” (IDEX – Paris-Saclay and Ecole Polytechnique).

## ■ ABBREVIATIONS

AMF, Alternating Magnetic Field  
BGNs, Bioactive Glass Nanoparticles  
BET, Brunauer–Emmett–Teller  
DMSO, Dimethyl Sulfoxide  
FTIR, Fourier Transform Infrared Spectroscopy  
HAC, Hydroxyapatite Apatite Carbonated  
HAp, Hydroxyapatite  
h-MSCs, Human Mesenchymal Stem Cells  
HRTEM, High-Resolution Transmission Electron Microscopy  
ICP-AES, Inductively Coupled Plasma-Atomic Emission Spectroscopy  
ILP, Intrinsic Loss Power  
MEM, minimum essential media  
MH, Magnetic Hyperthermia  
 $M_s$ , Saturation Magnetization  
MTT, 3-(4,5-dimethylthiazol-2-yl)-2,5-diphenyl tetrazolium bromide  
NPs, Nanoparticles  
OD, Optical Density  
PBS, Phosphate Buffer Saline  
SAR, Specific Absorption Rate  
SBF, Simulated Body Fluid  
SPIONs, Superparamagnetic Iron oxide Nanoparticles  
 $T_B$ , Blocking Temperature  
TEM, Transmission Electron Microscopy  
TEOS, Tetraethyl Orthosilicate  
WHO, World Health Organization  
XRD, X-Ray Diffraction  
ZFC-FC, Zero-Field Cooled-Field Cooled.

## ■ REFERENCES

(1) Hiraga, T. Bone Metastasis: Interaction between Cancer Cells and Bone Microenvironment. *J. Oral Biosci.* **2019**, *61*, 95–98.

- (2) Mundy, G. R. Metastasis to Bone: Causes, Consequences and Therapeutic Opportunities. *Nat. Rev. Cancer* **2002**, *2*, 584–593.
- (3) Coleman, R. E. Clinical Features of Metastatic Bone Disease and Risk of Skeletal Morbidity. *Clin. Cancer Res.* **2006**, *12*, 6243s–6249s.
- (4) Iñiguez-Ariza, N. M.; Bible, K. C.; Clarke, B. L. Bone Metastases in Thyroid Cancer. *J. Bone Oncol.* **2020**, *21*, 100282.
- (5) Willeumier, J. J.; van der Linden, Y. M.; Dijkstra, P. D. S. Lack of Clinical Evidence for Postoperative Radiotherapy after Surgical Fixation of Impending or Actual Pathologic Fractures in the Long Bones in Patients with Cancer; a Systematic Review. *Radiother. Oncol.* **2016**, *121*, 138–142.
- (6) Petca, R.; Gavrilu, S.; Burnei, G. Retrospective Clinicopathological Study of Malignant Bone Tumors in Children and Adolescents in Romania – Single Center Experience. *J. Med. Life* **2016**, *9*, 205–210.
- (7) Pankhurst, Q. A.; Connolly, J.; Jones, S. K.; Dobson, J. Applications of Magnetic Nanoparticles in Biomedicine. *J. Phys. Appl. Phys.* **2003**, *36*, R167–R181.
- (8) Kumar, C. S. S. R.; Mohammad, F. Magnetic Nanomaterials for Hyperthermia-Based Therapy and Controlled Drug Delivery. *Adv. Drug Delivery Rev.* **2011**, *63*, 789–808.
- (9) Cruz, M. M.; Ferreira, L. P.; Alves, A. F.; Mendo, S. G.; Ferreira, P.; Godinho, M.; Carvalho, M. D. Nanoparticles for Magnetic Hyperthermia. In *Nanostructures for Cancer Therapy*; Ficaí, A.; Grumezescu, A. M., Eds.; Micro and Nano Technologies; Elsevier, 2017; 485–511. DOI: 10.1016/B978-0-323-46144-3.00019-2.
- (10) Blanco-Andujar, C.; Walter, A.; Cotin, G.; Bordeianu, C.; Mertz, D.; Felder-Flesch, D.; Begin-Colin, S. Design of Iron Oxide-Based Nanoparticles for MRI and Magnetic Hyperthermia. *Nanomed.* **2016**, *11*, 1889–1910.
- (11) Gilchrist, R. K.; Medal, R.; Shorey, W. D.; Hanselman, R. C.; Parrott, J. C.; Taylor, C. B. Selective Inductive Heating of Lymph Nodes. *Ann. Surg.* **1957**, *146*, 596–606.
- (12) Figuerola, A.; Di Corato, R.; Manna, L.; Pellegrino, T. From Iron Oxide Nanoparticles towards Advanced Iron-Based Inorganic Materials Designed for Biomedical Applications. *Pharmacol. Res.* **2010**, *62*, 126–143.
- (13) Laurent, S.; Forge, D.; Port, M.; Roch, A.; Robic, C.; Vander Elst, L.; Muller, R. N. Magnetic Iron Oxide Nanoparticles: Synthesis, Stabilization, Vectorization, Physicochemical Characterizations, and Biological Applications. *Chem. Rev.* **2008**, *108*, 2064–2110.
- (14) Fu, R.; Yan, Y. Y.; Roberts, C. Study of the Effect of Dipole Interactions on Hyperthermia Heating the Cluster Composed of Superparamagnetic Nanoparticles. *AIP Adv.* **2015**, *5*, 127232.
- (15) Thiesen, B.; Jordan, A. Clinical Applications of Magnetic Nanoparticles for Hyperthermia. *Int. J. Hyperthermia* **2008**, *24*, 467–474.
- (16) Hench, L. L.; Splinter, R. J.; Allen, W. C.; Greenlee, T. K. Bonding Mechanisms at the Interface of Ceramic Prosthetic Materials. *J. Biomed. Mater. Res.* **1971**, *5*, 117–141.
- (17) Jones, J. R. Reprint of: Review of Bioactive Glass: From Hench to Hybrids. *Acta Biomater.* **2015**, *23*, S53–S82.
- (18) Sepulveda, P.; Jones, J. R.; Hench, L. L. Characterization of Melt-Derived 45S5 and Sol-Gel-Derived 58S Bioactive Glasses. *J. Biomed. Mater. Res.* **2001**, *58*, 734–740.
- (19) Fan, J. P.; Kalia, P.; Di Silvio, L.; Huang, J. In Vitro Response of Human Osteoblasts to Multi-Step Sol-Gel Derived Bioactive Glass Nanoparticles for Bone Tissue Engineering. *Mater. Sci. Eng. C* **2014**, *36*, 206–214.
- (20) Lei, B.; Chen, X.; Han, X.; Zhou, J. Versatile Fabrication of Nanoscale Sol-Gel Bioactive Glass Particles for Efficient Bone Tissue Regeneration. *J. Mater. Chem.* **2012**, *22*, 16906–16913.
- (21) Oonishi, H.; Hench, L. L.; Wilson, J.; Sugihara, F.; Tsuji, E.; Kushitani, S.; Iwaki, H. Comparative Bone Growth Behavior in Granules of Bioceramic Materials of Various Sizes. *J. Biomed. Mater. Res.* **1999**, *44*, 31–43.
- (22) Oonishi, H.; Kushitani, S.; Yasukawa, E.; Iwaki, H.; Hench, L. L.; Wilson, J.; Tsuji, E.; Sugihara, T. Particulate Bioglass Compared With Hydroxyapatite as a Bone Graft Substitute. *Clin. Orthop. Relat. Res.* **1997**, *334*, 316–325.
- (23) Wheeler, D. L.; Eschbach, E. J.; Hoellrich, R. G.; Montfort, M. J.; Chamberland, D. L. Assessment of Resorbable Bioactive Material for Grafting of Critical-Size Cancellous Defects. *J. Orthop. Res.* **2000**, *18*, 140–148.
- (24) Bretcanu, O.; Verné, E.; Coisson, M.; Tiberto, P.; Allia, P. Magnetic Properties of the Ferrimagnetic Glass-Ceramics for Hyperthermia. *J. Magn. Magn. Mater.* **2006**, *305*, S29–S33.
- (25) Wang, Y. Y.; Li, B.; Luo, W. Q.; Cao, F. Bioactivity of Fe<sub>2</sub>O<sub>3</sub>-CaO-SiO<sub>2</sub> Glass Ceramics Modified through the Addition of P<sub>2</sub>O<sub>5</sub> and TiO<sub>2</sub>. *Ceram. Int.* **2017**, *43*, 6738–6745.
- (26) Abbasi, M.; Hashemi, B.; Shokrollahi, H. Investigating in Vitro Bioactivity and Magnetic Properties of the Ferrimagnetic Bioactive Glass-Ceramic Fabricated Using Soda-Lime-Silica Waste Glass. *J. Magn. Magn. Mater.* **2014**, *356*, 5–11.
- (27) Vichery, C.; Maurin, I.; Bonville, P.; Boilot, J.-P.; Gacoin, T. Influence of Protected Annealing on the Magnetic Properties of  $\gamma$ -Fe<sub>2</sub>O<sub>3</sub> Nanoparticles. *J. Phys. Chem. C* **2012**, *116*, 16311–16318.
- (28) Hajdú, A.; Illés, E.; Tombác, E.; Borbáth, I. Surface Charging, Polyanionic Coating and Colloid Stability of Magnetite Nanoparticles. *Colloids Surf. Physicochem. Eng. Asp.* **2009**, *347*, 104–108.
- (29) Kokubo, T.; Takadama, H. How Useful Is SBF in Predicting in Vivo Bone Bioactivity? *Biomaterials* **2006**, *27*, 2907–2915.
- (30) Boistelle, R.; Astier, J. P. Crystallization Mechanisms in Solution. *J. Cryst. Growth* **1988**, *90*, 14–30.
- (31) Jolivet, J.-P. *De La Solution à l'oxyde: Condensation Des Cations En Solution Aqueuse; Chimie de Surface Des Oxydes*, Inter édition.; CNRS, 1994.
- (32) Baumgartner, J.; Dey, A.; Bomans, P. H. H.; Le Coadou, C.; Fratzl, P.; Sommerdijk, N. A. J. M.; Faivre, D. Nucleation and Growth of Magnetite from Solution. *Nat. Mater.* **2013**, *12*, 310–314.
- (33) Morales, M. P.; Veintemillas-Verdaguer, S.; Montero, M. I.; Serna, C. J.; Roig, A.; Casas, L.; Martínez, B.; Sandiumenge, F. Surface and Internal Spin Canting in  $\gamma$ -Fe<sub>2</sub>O<sub>3</sub> Nanoparticles. *Chem. Mater.* **1999**, *11*, 3058–3064.
- (34) Labbaf, S.; Tsigkou, O.; Müller, K. H.; Stevens, M. M.; Porter, A. E.; Jones, J. R. Spherical Bioactive Glass Particles and Their Interaction with Human Mesenchymal Stem Cells in Vitro. *Biomaterials* **2011**, *32*, 1010–1018.
- (35) de Oliveira, A. A. R.; de Souza, D. A.; Dias, L. L. S.; de Carvalho, S. M.; Mansur, H. S.; de Pereira, M. Synthesis, Characterization and Cytocompatibility of Spherical Bioactive Glass Nanoparticles for Potential Hard Tissue Engineering Applications. *Biomed. Mater.* **2013**, *8*, No. 025011.
- (36) Wu, C.; Fan, W.; Chang, J. Functional Mesoporous Bioactive Glass Nanospheres: Synthesis, High Loading Efficiency, Controllable Delivery of Doxorubicin and Inhibitory Effect on Bone Cancer Cells. *J. Mater. Chem. B* **2013**, *1*, 2710–2718.
- (37) Kesse, X.; Vichery, C.; Nedelec, J.-M. Deeper Insights into a Bioactive Glass Nanoparticle Synthesis Protocol To Control Its Morphology, Dispersibility, and Composition. *ACS Omega* **2019**, *4*, 5768–5775.
- (38) Kesse, X.; Vichery, C.; Jacobs, A.; Descamps, S.; Nedelec, J.-M. Unravelling the Impact of Calcium Content on the Bioactivity of Sol-Gel-Derived Bioactive Glass Nanoparticles. *ACS Appl. Bio Mater.* **2020**, *3*, 1312–1320.
- (39) Ma, D.; Veres, T.; Clime, L.; Normandin, F.; Guan, J.; Kingston, D.; Simard, B. Superparamagnetic FexOy@SiO<sub>2</sub> Core-Shell Nanostructures: Controlled Synthesis and Magnetic Characterization. *J. Phys. Chem. C* **2007**, *111*, 1999–2007.
- (40) Zhang, Y.; Liu, Y.; Li, M.; Lu, S.; Wang, J. The Effect of Iron Incorporation on the in Vitro Bioactivity and Drug Release of Mesoporous Bioactive Glasses. *Ceram. Int.* **2013**, *39*, 6591–6598.
- (41) Li, X.; Wang, X.; Hua, Z.; Shi, J. One-Pot Synthesis of Magnetic and Mesoporous Bioactive Glass Composites and Their Sustained Drug Release Property. *Acta Mater.* **2008**, *56*, 3260–3265.
- (42) Wu, C.; Fan, W.; Zhu, Y.; Gelinsky, M.; Chang, J.; Cuniberti, G.; Albrecht, V.; Friis, T.; Xiao, Y. Multifunctional Magnetic

Mesoporous Bioactive Glass Scaffolds with a Hierarchical Pore Structure. *Acta Biomater.* **2011**, *7*, 3563–3572.

(43) Zhu, Y.; Shang, F.; Li, B.; Dong, Y.; Liu, Y.; Lohe, M. R.; Hanagata, N.; Kaskel, S. Magnetic Mesoporous Bioactive Glass Scaffolds: Preparation, Physicochemistry and Biological Properties. *J. Mater. Chem. B* **2013**, *1*, 1279–1288.

(44) Liu, Y.-Z.; Li, Y.; Yu, X.-B.; Liu, L.-N.; Zhu, Z.-A.; Guo, Y.-P. Drug Delivery Property, Bactericidal Property and Cytocompatibility of Magnetic Mesoporous Bioactive Glass. *Mater. Sci. Eng. C* **2014**, *41*, 196–205.

(45) Pereira, A. M.; Pereira, C.; Silva, A. S.; Schmool, D. S.; Freire, C.; Grenèche, J.-M.; Araújo, J. P. Unravelling the Effect of Interparticle Interactions and Surface Spin Canting in  $\gamma$ -Fe<sub>2</sub>O<sub>3</sub>@SiO<sub>2</sub> Superparamagnetic Nanoparticles. *J. Appl. Phys.* **2011**, *109*, 114319.

(46) Tartaj, P.; González-Carreño, T.; Serna, C. J. Magnetic Behavior of  $\gamma$ -Fe<sub>2</sub>O<sub>3</sub> Nanocrystals Dispersed in Colloidal Silica Particles. *J. Phys. Chem. B* **2003**, *107*, 20–24.

(47) Papaefthymiou, G. C.; Devlin, E.; Simopoulos, A.; Yi, D. K.; Riduan, S. N.; Lee, S. S.; Ying, J. Y. Interparticle Interactions in Magnetic Core/Shell Nanoarchitectures. *Phys. Rev. B* **2009**, *80*, No. 024406.

(48) Kallumadil, M.; Tada, M.; Nakagawa, T.; Abe, M.; Southern, P.; Pankhurst, Q. A. Suitability of Commercial Colloids for Magnetic Hyperthermia. *J. Magn. Magn. Mater.* **2009**, *321*, 1509–1513.

(49) Périgo, E. A.; Hemery, G.; Sandre, O.; Ortega, D.; Garaio, E.; Plazaola, F.; Teran, F. J. Fundamentals and Advances in Magnetic Hyperthermia. *Appl. Phys. Rev.* **2015**, *2*, No. 041302.

(50) Serantes, D.; Simeonidis, K.; Angelakeris, M.; Chubykalo-Fesenko, O.; Marciello, M.; del Morales, M. P.; Baldomir, D.; Martínez-Boubeta, C. Multiplying Magnetic Hyperthermia Response by Nanoparticle Assembling. *J. Phys. Chem. C* **2014**, *118*, 5927–5934.

(51) Martínez-Boubeta, C.; Simeonidis, K.; Makridis, A.; Angelakeris, M.; Iglesias, O.; Guardia, P.; Cabot, A.; Yedra, L.; Estradé, S.; Peiró, F.; Saghi, Z.; Midgley, P. A.; Conde-Leborán, I.; Serantes, D.; Baldomir, D. Learning from Nature to Improve the Heat Generation of Iron-Oxide Nanoparticles for Magnetic Hyperthermia Applications. *Sci. Rep.* **2013**, *3*, 1652.

(52) Lartigue, L.; Hugounenq, P.; Alloyeau, D.; Clarke, S. P.; Lévy, M.; Bacri, J.-C.; Bazzi, R.; Brougham, D. F.; Wilhelm, C.; Gazeau, F. Cooperative Organization in Iron Oxide Multi-Core Nanoparticles Potentiates Their Efficiency as Heating Mediators and MRI Contrast Agents. *ACS Nano* **2012**, *6*, 10935–10949.

(53) Hugounenq, P.; Levy, M.; Alloyeau, D.; Lartigue, L.; Dubois, E.; Cabuil, V.; Ricolleau, C.; Roux, S.; Wilhelm, C.; Gazeau, F.; Bazzi, R. Iron Oxide Monocrystalline Nanoflowers for Highly Efficient Magnetic Hyperthermia. *J. Phys. Chem. C* **2012**, *116*, 15702–15712.

(54) Ovejero, J. G.; Cabrera, D.; Carrey, J.; Valdivielso, T.; Salas, G.; Teran, F. J. Effects of Inter- and Intra-Aggregate Magnetic Dipolar Interactions on the Magnetic Heating Efficiency of Iron Oxide Nanoparticles. *Phys. Chem. Chem. Phys.* **2016**, *18*, 10954–10963.

(55) Etheridge, M. L.; Hurley, K. R.; Zhang, J.; Jeon, S.; Ring, H. L.; Hogan, C.; Haynes, C. L.; Garwood, M.; Bischof, J. C. Accounting for Biological Aggregation in Heating and Imaging of Magnetic Nanoparticles. *Technology* **2014**, *02*, 214–228.

(56) Coral, D. F.; Mendoza Zélis, P.; Marciello, M.; del Morales, M. P.; Craievich, A.; Sánchez, F. H.; Fernández van Raap, M. B. Effect of Nanoclustering and Dipolar Interactions in Heat Generation for Magnetic Hyperthermia. *Langmuir* **2016**, *32*, 1201–1213.

(57) Gonzalez-Fernandez, M. A.; Torres, T. E.; Andrés-Vergés, M.; Costo, R.; de la Presa, P.; Serna, C. J.; Morales, M. P.; Marquina, C.; Ibarra, M. R.; Goya, G. F. Magnetic Nanoparticles for Power Absorption: Optimizing Size, Shape and Magnetic Properties. *J. Solid State Chem.* **2009**, *182*, 2779–2784.

(58) Erné, B. H.; Butter, K.; Kuipers, B. W. M.; Vroege, G. J. Rotational Diffusion in Iron Ferrofluids. *Langmuir* **2003**, *19*, 8218–8225.

(59) Wang, X.; Gu, H.; Yang, Z. The Heating Effect of Magnetic Fluids in an Alternating Magnetic Field. *J. Magn. Magn. Mater.* **2005**, *293*, 334–340.

(60) Deatsch, A. E.; Evans, B. A. Heating Efficiency in Magnetic Nanoparticle Hyperthermia. *J. Magn. Magn. Mater.* **2014**, *354*, 163–172.

(61) Múzquiz-Ramos, E. M.; Cortés-Hernández, D. A.; Escobedo-Bocardo, J. C.; Zugasti-Cruz, A.; Ramírez-Gómez, X. S.; Osuna-Alarcón, J. G. In Vitro and in Vivo Biocompatibility of Apatite-Coated Magnetite Nanoparticles for Cancer Therapy. *J. Mater. Sci. Mater. Med.* **2013**, *24*, 1035–1041.

(62) Kokubo, T.; Kim, H.-M.; Kawashita, M. Novel Bioactive Materials with Different Mechanical Properties. *Biomaterials* **2003**, *24*, 2161–2175.

(63) Zheng, K.; Solodovnyk, A.; Li, W.; Goudouri, O.-M.; Stähli, C.; Nazhat, S. N.; Boccaccini, A. R. Aging Time and Temperature Effects on the Structure and Bioactivity of Gel-Derived 45SS Glass-Ceramics. *J. Am. Ceram. Soc.* **2015**, *98*, 30–38.

(64) Balamurugan, A.; Sockalingum, G.; Michel, J.; Fauré, J.; Banchet, V.; Wortham, L.; Bouthors, S.; Laurent-Maquin, D.; Balossier, G. Synthesis and Characterisation of Sol Gel Derived Bioactive Glass for Biomedical Applications. *Mater. Lett.* **2006**, *60*, 3752–3757.

(65) Zhu, Y.; Kaskel, S. Comparison of the in Vitro Bioactivity and Drug Release Property of Mesoporous Bioactive Glasses (MBGs) and Bioactive Glasses (BGs) Scaffolds. *Microporous Mesoporous Mater.* **2009**, *118*, 176–182.

(66) Ebisawa, Y.; Kokubo, T.; Ohura, K.; Yamamuro, T. Bioactivity of Fe<sub>2</sub>O<sub>3</sub>-Containing CaO-SiO<sub>2</sub> Glasses: In Vitro Evaluation. *J. Mater. Sci. Mater. Med.* **1993**, *4*, 225–232.

(67) Ohura, K.; Nakamura, T.; Yamamuro, T.; Ebisawa, Y.; Kokubo, T.; Kotoura, Y.; Oka, M. Bioactivity of CaO-SiO<sub>2</sub> Glasses Added with Various Ions. *J. Mater. Sci. Mater. Med.* **1992**, *3*, 95–100.